Acta Materialia 200 (2020) 389–403

Contents lists available at ScienceDirect

Acta Materialia

journal homepage: www.elsevier.com/locate/actamat

Phase boundary segregation-induced strengthening and discontinuous yielding in ultrafine-grained duplex medium-Mn steels

Yan Ma[a,b,*], Binhan Sun[b,*], Alexander Schökel[c], Wenwen Song[a], Dirk Ponge[b], Dierk Raabe[b], Wolfgang Bleck[a]

[a] Steel Institute, RWTH Aachen University, Intzestraße 1, 52072 Aachen, Germany
[b] Department of Microstructure Physics and Alloy Design, Max-Planck-Institut für Eisenforschung GmbH, Max-Planck-Straße 1, 40237 Düsseldorf, Germany
[c] Deutsches Elektronen Synchrotron (DESY), Notkestraße 85, 22607 Hamburg, Germany

ARTICLE INFO

Article history:
Received 25 May 2020
Revised 24 August 2020
Accepted 2 September 2020
Available online 12 September 2020

Keywords:
Medium-Mn steels
Phase boundary
Segregation engineering
Strengthening
Discontinuous yielding

ABSTRACT

The combination of different phase constituents to realize a mechanical composite effect for superior strength-ductility synergy has become an important strategy in microstructure design in advanced high-strength steels. Introducing multiple phases in the microstructure essentially produces a large number of phase boundaries. Such hetero-interfaces affect the materials in various aspects such as dislocation activity and damage formation. However, it remains a question whether the characteristics of phase boundaries, such as their chemical decoration states, would also have an impact on the mechanical behavior in multiphase steels. Here we reveal a phase boundary segregation-induced strengthening effect in ultrafine-grained duplex medium-Mn steels. We found that the carbon segregation at ferrite-austenite phase boundaries can be manipulated by adjusting the cooling conditions after intercritical annealing. Such phase boundary segregation in the investigated steels resulted in a yield strength enhancement by 100–120 MPa and simultaneously promoted discontinuous yielding. The sharp carbon segregation at the phase boundaries impeded interfacial dislocation emission, thus increasing the stress required to activate such dislocation nucleation process and initiate plastic deformation. This observation suggests that the enrichment of carbon at the phase boundaries can enhance the energy barrier for dislocation emission, which provides a favorable condition for plastic flow avalanches and thus discontinuous yielding. These findings extend the current understanding of the yielding behavior in medium-Mn steels, and more importantly, shed light on utilizing and manipulating phase boundary segregation to improve the mechanical performance of multiphase metallic materials.

1. Introduction

The development and application of advanced high-strength steels (AHSSs) are of prime interest in the automotive industry for attempts to reduce the weight of body-in-white and thus the fuel economy as well as to improve vehicle safety [1]. Numerous AHSSs have been proposed in the last decades to obtain high strength (tensile strength above ~600 MPa) and simultaneously ensure good formability [1–3]. Due to economic constraints and better recycling, most recent alloy design concepts avoid using expensive alloying elements or high alloying contents [4]. Instead, compositionally lean alloys are targeted and thermomechanical treatments are used to produce multiphase microstructures with balanced phase stability and a high density of interfaces [5,6]. This approach enables the utilization of a large variety of accessible phase constituents (e.g. ferrite, austenite, martensite, and bainite) in steels with the aim to utilize a mechanical composite effect for achieving a superior strength-ductility synergy [7–10]. Due to the multiple phases, a large number of phase boundaries characterizes such microstructures. These hetero-interfaces differ from random high-angle grain boundaries in terms of their interface structure and chemistry [11,12]. Another feature associated with the presence of phase boundaries is the enhanced stress/strain concentrations at these interfaces due to the typically high mechanical contrast between adjacent phases [13–15]. These factors have been used to explain the influence of phase boundaries on the mechanical behavior in multiphase AHSSs, such as the onset and pattern of yielding [16,17], damage tolerance [17-19], as well as hydrogen trapping and embrittlement [20,21].

* Corresponding authors at: Department of Microstructure Physics and Alloy Design, Max-Planck-Institut für Eisenforschung GmbH, Max-Planck-Straße 1, 40237 Düsseldorf, Germany.
E-mail addresses: y.ma@mpie.de (Y. Ma), b.sun@mpie.de (B. Sun).

https://doi.org/10.1016/j.actamat.2020.09.007
1359-6454/

Table 1
Chemical composition of the investigated medium-Mn steel.

Element	Fe	C	Si	Mn	P	S	Al
wt.%	Bal.	0.064	0.2	11.7	0.006	0.003	2.9
at.%	Bal.	0.287	0.4	11.5	0.010	0.005	5.8

Recently, medium-Mn steels with 3–12 wt.% Mn content have attracted immense attention due to their excellent mechanical performance (product of tensile strength and total elongation up to ~70 GPa% [22]), which qualifies this type of steel as a promising candidate material for the third generation of AHSSs [22–24]. Such steels are commonly processed by intercritical annealing to produce a ferrite-austenite two-phase microstructure [22–25]. They usually possess an ultrafine grain size (ranging from the submicron level to a few micrometers), which could result from the austenite reversion from a fine martensitic matrix and the associated sluggish manganese partitioning during the intercritical annealing [26]. Such a microstructure leads to a large area fraction of ferrite-austenite phase boundaries. In many cases, this type of interface even becomes the dominant and thus most relevant type of planar defects for the mechanical behavior in medium-Mn steels [16]. In our previous study of an intercritically annealed medium-Mn steel (Fe-10Mn-3Al-1Si-0.2C, in wt.%) [16], we observed clear signs of dislocation emission from the ferrite-austenite phase boundaries in the steel's early yielding stage. The large phase boundary area can provide a high density of dislocation sources, entailing the rapid multiplication of mobile dislocations. This mechanism was proposed to be the major reason for the discontinuous yielding phenomenon in medium-Mn steels [16]. It also gives proof of the important role of phase boundaries in the mechanical behavior in multiphase steels. It remains an open question, though, whether the characteristics of these hetero-interfaces such as the local chemistry also affect the yielding behavior in medium-Mn steels. The chemical decoration state of grain boundaries and its influence on yielding properties (e.g. yield strength and Hall-Petch coefficient K_y) have been documented in several single-phase steels [27–30]. However, corresponding investigations on phase boundaries have been rarely reported.

In the present study, we investigate the influence of phase boundary segregation on the yielding behavior in ultrafine-grained duplex medium-Mn steels. The carbon decoration of the ferrite-austenite phase boundaries is controlled by adjusting the cooling conditions after intercritical annealing. Its influence on the initiation of plastic deformation in both phases and the resulting macroscopic yielding behavior (including yield strength and the prevalence of continuous or discontinuous yielding) is analyzed using a multiscale microstructural and mechanical characterization strategy. The underlying mechanisms of carbon segregation at the phase boundaries and its effect on the associated dislocation emission in the early yielding stages are discussed.

2. Experimental methods

2.1. Material and processing

A low-carbon medium-Mn steel with the chemical composition of Fe-11.7Mn-2.9Al-0.064C (in wt.%, Table 1) was investigated in the current study. Casting and hot-rolling procedures were described elsewhere [31]. The total thickness reduction imposed by cold rolling was ~50% and the final thickness of the cold-rolled sheet was 1.25 mm. Tensile test specimens were prepared along the rolling direction and subjected to intercritical annealing in a salt bath at 700 °C for 2 hours. Under such an annealing condition, the thermal equilibrium was fully realized [32]. After intercritical annealing, the specimens were either directly quenched into water or cooled in air. The temperature profiles of these two cooling procedures were measured by a thermocouple attached to the surface of the specimens and the results are shown in Fig. 1. The very high cooling rate achieved by water quenching (~205 °C/s) allows freezing the microstructure and the elemental distribution formed during annealing at 700 °C. In contrast, the relatively low cooling rate in air, especially when below 400 °C (lower than 3.5 °C/s, Fig. 1), provides enough time for short-distance diffusion of the interstitial carbon atoms, thus fulfilling the kinetic conditions for interfacial segregation. The water-quenched and air-cooled specimens are referred to as WQ and AC samples, respectively, hereafter.

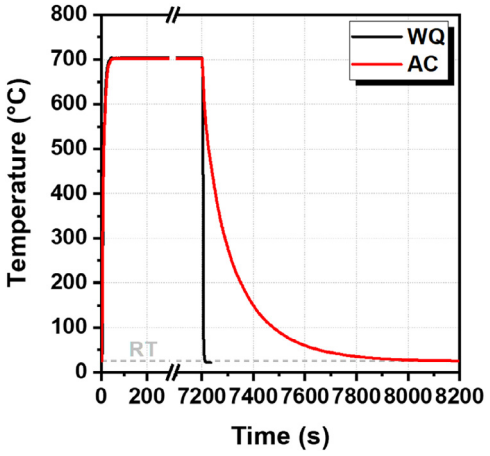

Fig. 1. Temperature profile of the intercritical annealing and cooling procedures imposed on the tensile specimens with the thickness of 1.25 mm. (WQ stands for water quenching, AC for air cooling, and RT for room temperature.)

2.2. Mechanical testing

The room-temperature mechanical properties were evaluated by quasi-static tensile tests, which were carried out according to the DIN EN ISO 6892-1 standard in a Z4204 tensile machine at an initial strain rate of ~1×10^{-3} s^{-1}. The gauge length and width of the tensile specimens were 20 mm and 6 mm, respectively. An optical strain measurement system with a video extensometer was employed for quantifying the specimens' strain. Three tests were repeated for each cooling condition for achieving reasonable statistics. The yield strength was determined as the upper yield point for the sample showing discontinuous yielding and the 0.2% offset strength for the case of continuous yielding. Digital image correlation (DIC) was used to characterize the local strain distribution and the formation of Lüders bands during tensile testing. A subsized tensile specimen with a gauge length of 4 mm and width of 2 mm was used for this purpose. DIC data were analyzed by the ARAMIS software.

2.3. Microstructural characterization

The microstructure of undeformed material and samples taken from interrupted tensile tests was characterized by a combination of electron backscatter diffraction (EBSD) and electron channeling contrast imaging (ECCI) techniques [33] (a JEOL JSM-6500F and a Zeiss Sigma 500 scanning electron microscope (SEM) for EBSD, and a Zeiss-Merlin SEM for ECCI). The step size for EBSD measurement was 50–60 nm. The acquired EBSD data (phase constituents, fractions, grain sizes, interfaces, and misorientation) were analyzed using the software OIM Analysis™ V8.0.

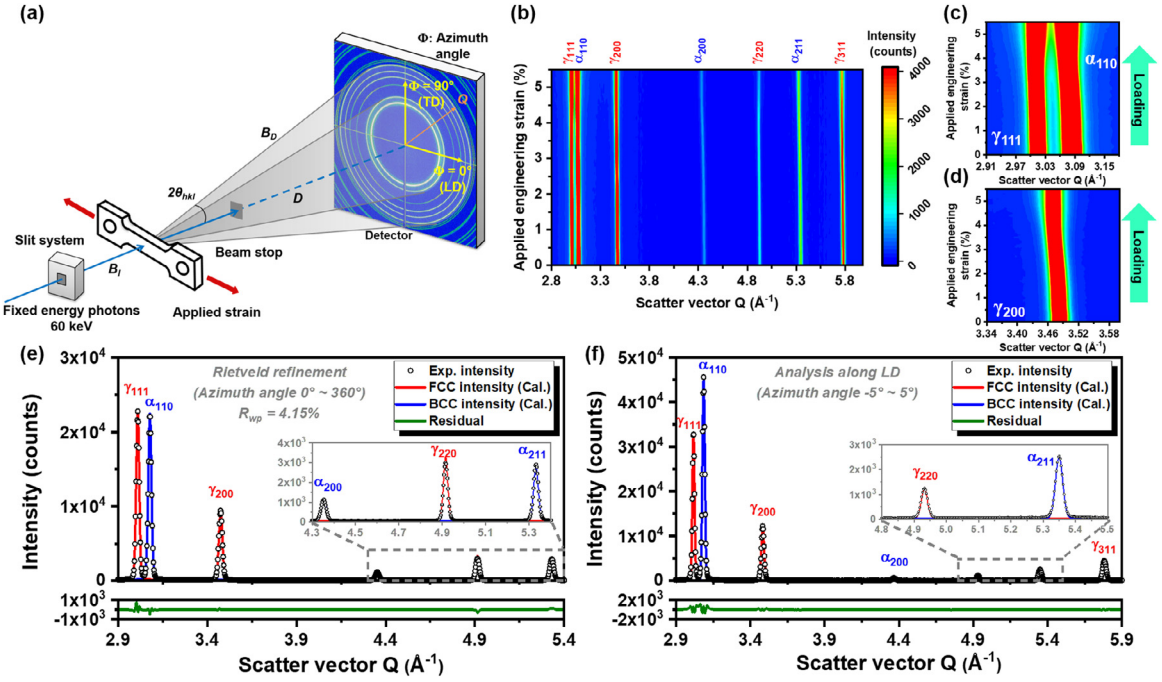

Fig. 2. (a) Schematic illustration of the setup of the *in situ* synchrotron high-energy X-ray diffraction experiment (B_I and B_D are the incident and diffracted beams, respectively; D is the detector distance between the sample and the two-dimensional detector; $2\theta_{hkl}$ is the angle between the incident and diffracted beams; Q is the scatter vector; LD stands for loading direction and TD for transverse direction); (b) Contour map of the intensity integrated over azimuth angle from -5° to 5° during loading of the water-quenched (WQ) specimen; (c) Magnified contour plot of peaks γ_{111} and α_{110} in (b); (d) Magnified contour plot of peak γ_{200} in (b); (e) Integrated diffraction profile (open dots) of the WQ specimen prior to loading over azimuth angle of 360° as a function of scatter vector Q and the corresponding fitted peaks (solid lines) using the Rietveld refinement method. (f) Integrated diffraction profile (open dots) over azimuth angle from -5° to 5° and the corresponding fitted peaks (solid lines) using the single peak fitting method.

2.4. Atom probe tomography

The near atomic-scale elemental distribution across phase boundaries was characterized by atom probe tomography (APT). The measurements were conducted using a Local Electrode Atom Probe 4000X HR instrument operated in laser-pulsing mode with an ultraviolet laser (wavelength 355 nm). The base temperature in the analysis chamber was maintained at 60 K. The frequency of the laser pulses and the laser energy were 250 kHz and 30 pJ, respectively. The APT samples were prepared using FEI® Helios^{TM} Nanolab^{TM} 660 dual-beam system. The analysis of the APT data was carried out using the IVAS 3.8.0 software package.

2.5. In situ *synchrotron high-energy X-ray diffraction*

In situ synchrotron high-energy X-ray diffraction (HEXRD) was employed mainly to investigate the micromechanical behavior of individual phases during tensile deformation. The HEXRD experiments were conducted at the Powder Diffraction and Total Scattering Beamline P02.1 of PETRA III at Deutsches Elektronen-Synchrotron (DESY) in Hamburg, Germany [34]. The beamline was operated at a fixed energy of 60 keV, supplying a monochromatic X-ray with a wavelength of ~0.207 Å. Fig. 2(a) illustrates the experimental setup of the *in situ* HEXRD experiments. A Kammrath & Weiss stress rig with a max load of 5 kN was placed between the incident beam and two-dimensional detector to perform the tensile deformation. Sub-sized tensile specimens with a gauge length of 12 mm and width of 2 mm were used. The tensile tests were carried out at room temperature with a constant crosshead speed corresponding to the initial strain rate of ~1 $\times$ 10^{-3} s^{-1}. The sample to detector distance was approx. one meter. The beam size of the incident beam was 0.6 mm $\times$ 0.6 mm. The large probing volume through sample thickness (1.25 mm) was able to include more than 255 million ultrafine grains with an average grain size of 1.5 µm. This large detection volume yielded reliable statistical information on the microstructure. The two-dimensional Debye-Scherrer patterns were recorded by a fast area detector Varex XRpad 4343CT (2880 pixels $\times$ 2880 pixels). In order to capture the time-resolved microstructure evolution during deformation, the HEXRD data were acquired with high frequency, namely one diffraction pattern per second.

For quantitative microstructure analysis, in terms of the fraction of individual phases and their initial lattice parameters, the recorded two-dimensional diffraction patterns were integrated over an azimuth angle of 360° into intensity-scattering vector (Q) plots using the Fit2D software [35]. The diffraction profiles were then analyzed by the Rietveld refinement method with the aid of the Materials Analysis Using Diffraction (MAUD) software [36]; the detailed procedures were documented elsewhere [37]. The goodness of the refinement can be evaluated by the weighted profile R-factor (R_{wp}). The R_{wp} value for all the refinements in the present work is below 7.5%, suggesting the high reliability of the refinement results. Fig. 2(e) demonstrates one example of the calculated diffraction profile using the Rietveld refinement. The diffraction peaks of γ-austenite (face-centered cubic, i.e. FCC, *Fm-3m* space group) and α-ferrite (body-centered cubic, i.e. BCC, *Im-3m* space group) were distinguished. The fitted diffraction profile (solid lines) showed a good agreement with the experimental diffraction data (open dots).

To investigate the micromechanical response of the individual phases upon deformation, the lattice strain along the loading direction was analyzed. The diffraction pattern was integrated in the section over an azimuth angle from -5° to 5°. The evolution of the integrated peaks upon loading is shown as a contour map in Fig. 2(b). The contour maps of the major crystallographic diffraction planes γ_{111} and α_{110}, as well as γ_{200}, are enlarged in Fig. 2(c)

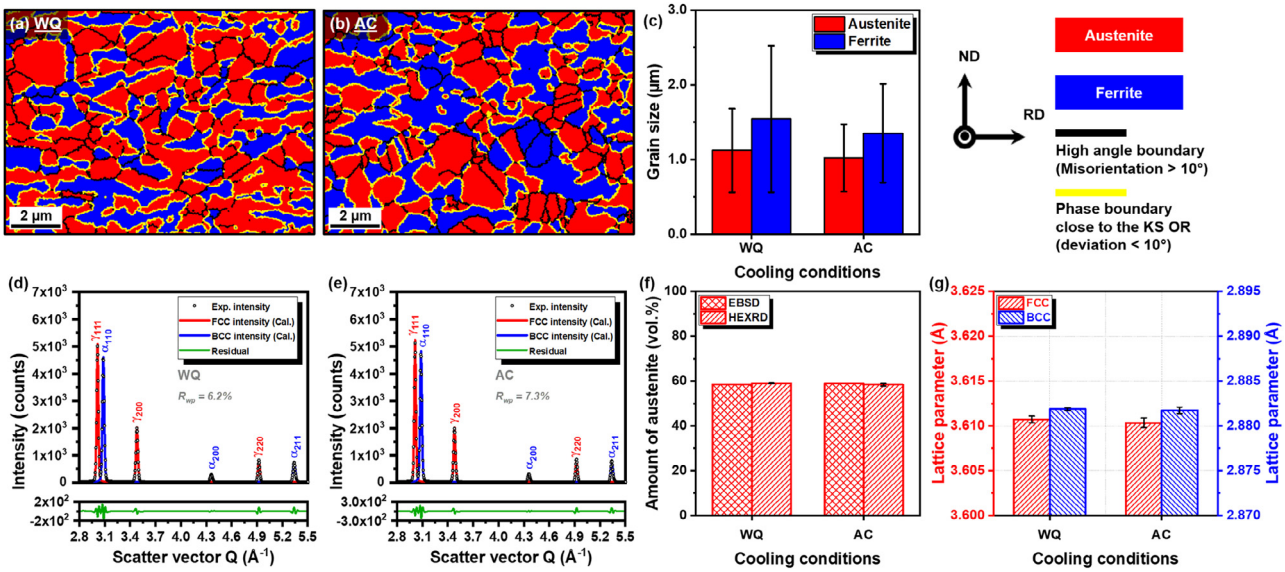

Fig. 3. Electron backscattered diffraction (EBSD) phase maps of (a) the water-quenched (WQ) sample and (b) the air-cooled (AC) sample (ND stands for normal direction, RD for rolling direction, and KS OR for Kurdjumov-Sachs orientation relationship); (c) Average grain size of the two specimens measured by EBSD; Synchrotron high-energy X-ray diffraction (HEXRD) profiles of (d) the WQ sample and (e) the AC sample; (f) The volume fraction of austenite determined by EBSD and HEXRD; (g) The lattice parameter of austenite and ferrite measured by HEXRD. (The HEXRD results were averaged over three measurements.)

and (d), respectively. The diffraction peaks shifted to the lower scatter vector values upon deformation, suggesting an increase in the lattice-plane spacing. To determine the precise interplanar spacing (d_{hkl}) of individual lattice planes, the integral diffraction peaks were then fitted by the single peak fitting method using the Gaussian function. An example of the fitting result is shown in Fig. 2(f). The lattice strain (ε_{hkl}) was calculated by the following equation [38]:

$$\varepsilon_{hkl} = \left(d^{\sigma}_{hkl} - d^{0}_{hkl}\right)/d^{0}_{hkl} \quad (1)$$

where d^{σ}_{hkl} and d^{0}_{hkl} are the lattice-plane spacing under loading and prior to loading, respectively.

Furthermore, the weighted average lattice strain ($\bar{\varepsilon}_{\mathrm{ph}}$) of individual phases was calculated as follows [38]:

$$\bar{\varepsilon}_{\mathrm{ph}} = (\bar{a}_{\sigma} - \bar{a}_{0})/\bar{a}_{0} \quad (2)$$

where $\bar{a}_{\sigma}$ and $\bar{a}_{0}$ are the weighted average lattice parameter under loading and prior to loading, respectively. The weighted average lattice parameter can be calculated by the following equation [38]:

$$\bar{a} = \sum_{hkl} f_{hkl} \cdot a_{hkl} \quad (3)$$

where f_{hkl} is the intensity fraction of the {hkl} reflection over all analyzed peaks; a_{hkl} is the lattice parameter calculated from the {hkl} reflection.

3. Results

3.1. Microstructure

The microstructure of the WQ and AC samples after intercritical annealing are shown in Fig. 3(a) and (b). Both showed an ultrafine-grained duplex microstructure consisting of α-ferrite and γ-austenite with an equiaxed grain morphology. Such two-phase microstructure was also validated by the HEXRD measurements (Fig. 3(d) and (e)). Carbide precipitation during cooling was likely suppressed due to the low carbon content and the addition of aluminum [39,40], thus no diffraction peaks of carbides can be found even in the AC sample. The average grain size of austenite and ferrite was similar for the two samples (1.1 μm for γ and 1.5 μm for α in the WQ specimen; 1.0 μm for γ and 1.4 μm for α in the AC specimen), Fig. 3(c). The fraction of austenite was also very similar for the two samples, as demonstrated by both EBSD (58.6 vol.% and 58.9 vol.% for the WQ and AC samples, respectively) and HEXRD results (59.0±0.2 vol.% and 58.4±0.7 vol.% for the WQ and AC samples, respectively), Fig. 3(f). The ultrafine grains in the two samples resulted in a high density of interfaces, as quantified by EBSD (Table 2). In particular, the ferrite-austenite phase boundaries constituted the major type of high-angle interface boundaries, with fractions of 72.6% and 66.1% for the WQ and AC specimens, respectively. The characteristics of these interfaces are important for the mechanical behavior, especially for the onset of plasticity (i.e. yielding) in this type of material, as will be shown in Sections 3.2 to 3.5. An approximate Kurdjumov-Sachs (KS) orientation relationship [41], characterized by $\{111\}_{\gamma}||\{110\}_{\alpha}$ and $<1\bar{1}0>_{\gamma}||<1\bar{1}1>_{\alpha}$, was predominantly observed between austenite grains and their adjacent ferrite grains, as highlighted by the yellow lines in Figs. 3(a) and (b). The lattice parameter of austenite and ferrite, determined by the HEXRD method, was also similar for the two samples (3.6107±0.0004 Å for γ and 2.8819±0.0002 Å for α in the WQ sample; 3.6104±0.0006 Å for γ and 2.8818±0.0004 Å for α in the AC sample), Fig. 3(g). This observation suggested no evident difference in the average carbon concentration of each phase between the two samples [42]. It can thus be concluded that the two samples upon different cooling procedures showed a high similarity of microstructural features, in terms of phase constituents, fractions, grain sizes, and grain morphologies.

3.2. Carbon segregation at the ferrite-austenite phase boundaries

The behavior of the solute element distribution across the α-γ phase boundaries observed in the two samples is shown in Fig. 4. In both specimens, γ-austenite was enriched in manganese and carbon, while α-ferrite was enriched in aluminum (Figs. 4(c) and (e)). This phenomenon was due to solute element partitioning occurring during intercritical annealing at 700 °C [43,44]. The APT data showed that the concentration of the solute elements in

Table 2
Length and relative fraction of different types of high-angle interface boundaries (HABs, misorientation angle > 10°) in the water-quenched (WQ) and air-cooled (AC) specimens based on electron backscattered diffraction measurements. (Probing area 20 × 25 μm², containing roughly 470 grains).

Type of boundaries	WQ specimen		AC specimen	
	Length (μm)	Relative fraction to HABs (%)	Length (μm)	Relative fraction to HABs (%)
High-angle boundaries	2120.0	100	2160.1	100
α-α grain boundaries	105.9	5.0	108.2	5.0
γ-γ grain boundaries	388.8	18.4	509.6	23.6
Σ3 twin boundaries in γ	85.6	4.0	114.5	5.3
α-γ phase boundaries	1539.7	72.6	1427.8	66.1

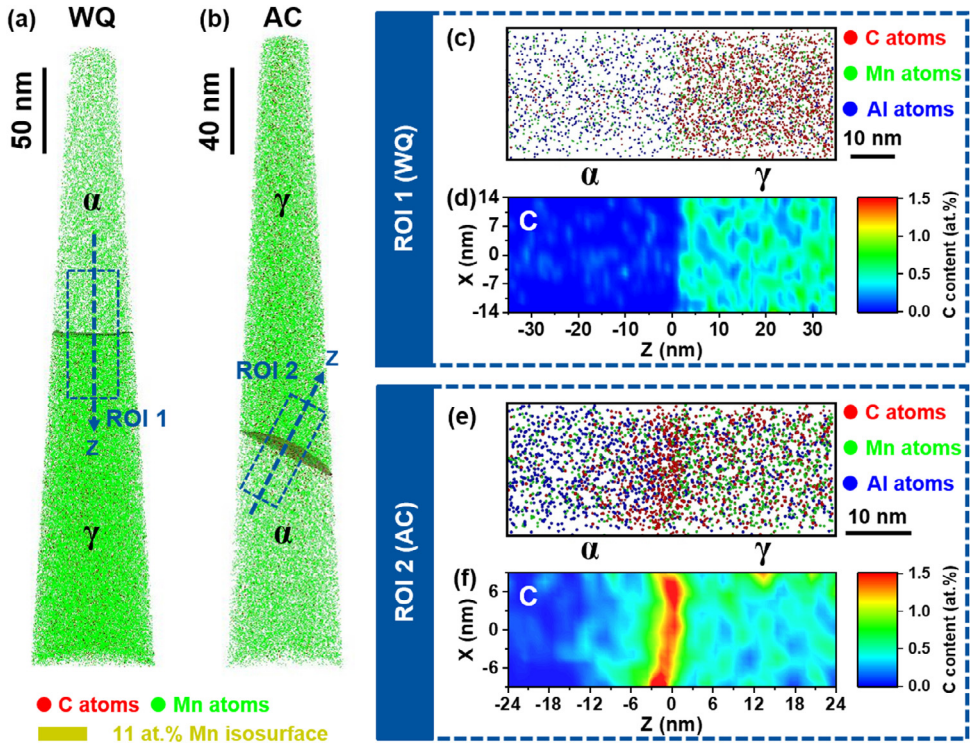

Fig. 4. Three-dimensional atom probe tomography maps of carbon and manganese in (a) the water-quenched (WQ) specimen and (b) the air-cooled (AC) specimen (The phase boundary is marked by an 11 at.% Mn iso-concentration surface.); (c) and (e) Distribution of carbon, manganese, and aluminum atoms in the vicinity of the ferrite-austenite phase boundary, taken from the selected region of interest (ROI) marked in (a) and (b), respectively (Note that the different sphere sizes in (c) and (e) are due to the different image magnification levels, as indicated by the scale bars.); (d) and (f) Corresponding two-dimensional concentration maps of carbon in the ROI in (a) and (b), respectively.

Table 3
Concentration of major elements in the matrix of ferrite and austenite in the water-quenched (WQ) and air-cooled (AC) specimens measured by atom probe tomography. (Average concentration in a region of the APT tip from 60 nm to 80 nm away from the interface.)

Element (at.%)	WQ specimen		AC specimen	
	Ferrite	Austenite	Ferrite	Austenite
Fe	85.02±0.55	81.16±0.65	84.84±0.80	79.97±0.87
Mn	6.99±0.26	14.03±0.36	6.95±0.49	14.88±0.49
Al	7.63±0.46	3.93±0.55	7.71±0.68	4.40±0.63
C	0.06±0.04	0.44±0.09	0.05±0.02	0.44±0.17

ferrite and austenite was similar for the two samples (Table 3). This observation suggested that the cooling conditions had negligible impact on overall elemental partitioning. However, the local carbon distribution at the α-γ phase boundaries was substantially influenced by the cooling condition, as illustrated by the two-dimensional carbon concentration maps in Fig. 4(d) and (f) and further by the one-dimensional carbon concentration profile in Fig. 5.

The phase boundary was marked by an 11 at.% Mn iso-concentration surface (Fig. 4), and the carbon concentration profile was plotted using the proximity histogram (proxigram) approach relative to the Mn iso-concentration surface [45] (Fig. 5). For the WQ specimen, no carbon enrichment was observed at the phase boundary (Fig. 4(d) and Fig. 5(a)). However, carbon enrichment was pronounced in the AC specimen (Fig. 4(f)), as revealed by the clear carbon spike at the phase boundary (see the carbon profile in Fig. 5(b)). Hereafter, the observed carbon enrichment at the phase boundary is referred to as carbon segregation following the terminology used in Ref. [46], even though the underlying mechanisms could be different from the segregation at grain boundaries, which will be discussed in Section 4.1.

The carbon spike was built up almost at the position of the original phase boundary (marked by the position of the 11 at.% Mn iso-concentration surface, i.e. 0 nm in Fig. 5(b)), with approx. 1 nm shift towards the ferrite. This result implied that (1) the interface migrated slightly towards the ferrite during air cooling, and (2) austenite decomposition was unlikely, which was expected to lead to the migration of the hetero-interface towards the austenite. The

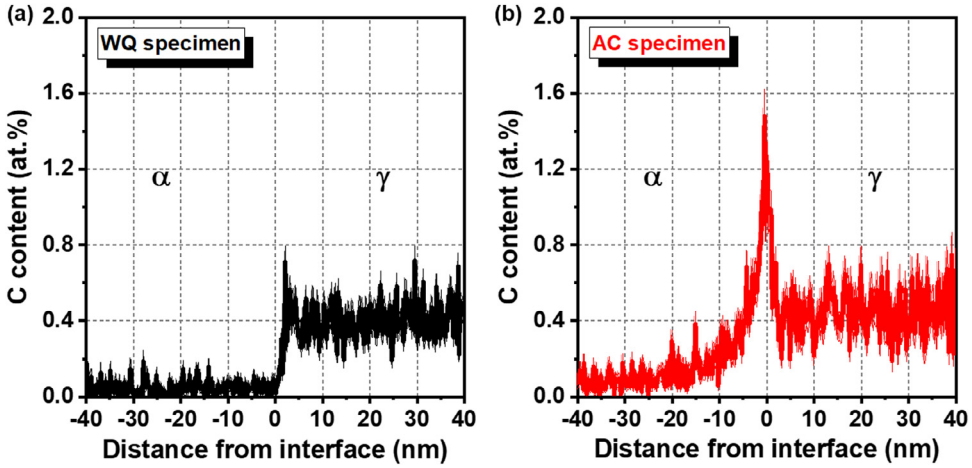

Fig. 5. Carbon concentration profiles relative to the position of the phase boundary in (a) the water-quenched (WQ) specimen and (b) the air-cooled (AC) specimen.

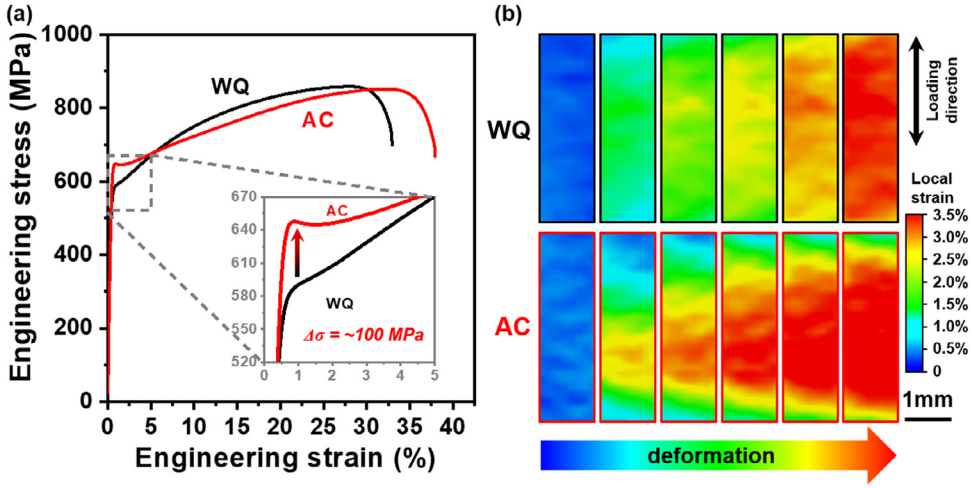

Fig. 6. (a) Engineering stress-strain curves of the water-quenched (WQ) and air-cooled (AC) specimens (the arrow indicates an increase in yield strength); (b) Local strain distribution covering the whole gauge section of the two specimens in the yielding stage.

concentration of the carbon spike for this sample was determined to be ~1.48 at.%, which was about five times higher than the nominal carbon content (0.29 at.%) of the material, as well as more than three times and 25 times higher than the carbon content within austenite (~0.44 at.%) and ferrite (~0.06 at.%), respectively. These clear differences in the carbon segregation behavior between the WQ and AC specimens was observed in all the probed APT tips containing phase boundaries (three APT tips for each cooling condition). Such a high degree of carbon segregation at the α-γ phase boundaries has not been reported before for ultrafine-grained duplex medium-Mn steels. Its origin will be discussed in Section 4.1.

3.3. Mechanical properties

The influence of the cooling condition on the tensile behavior is shown in Fig. 6. The WQ specimen demonstrated a clear continuous yielding behavior, i.e., no upper and lower yield points appeared in the tensile curve (Fig. 6(a)) and no localized deformation bands were found over the whole yielding stage (as shown in the DIC results in Fig. 6(b)). In contrast, a yield drop was observed in the AC specimen (Fig. 6(a)), despite its small value (the difference between upper and lower yield points was ~3 MPa). Also, the DIC results showed the formation of a Lüders band with a local strain of ~3%. The band nucleated roughly at the upper yield point and propagated towards both sides along the tensile axis during deformation (Fig. 6(b)). During the band propagation, the plastic deformation was localized, and thus the macroscopic stress was maintained almost constant until the band passed through the entire tensile gauge. These observations revealed a clear discontinuous yielding phenomenon for the AC sample. Furthermore, it was observed that the AC sample possessed a higher yield strength compared with the WQ sample (656±17 MPa for the AC sample vs. 556±14 MPa for the WQ sample). Such a difference in the yield strength and macroscopic yielding behavior between the two samples is deemed to be related to the substantial carbon segregation found at the α-γ phase boundaries (Figs. 4 and 5), as will be discussed in Section 4.2.

3.4. Yielding behavior of individual phases tracked by in situ synchrotron HEXRD

The deformation behavior of individual phases was further compared between the two samples, with particular attention to the initial regime of the plastic deformation (i.e. yielding). Such analysis was realized by *in situ* synchrotron HEXRD experiments, which allows tracking the deformation-driven change in lattice strain with good statistical evidence. The possible austenite-to-martensite phase transformation during yielding could also be detected by HEXRD in the yielding stage.

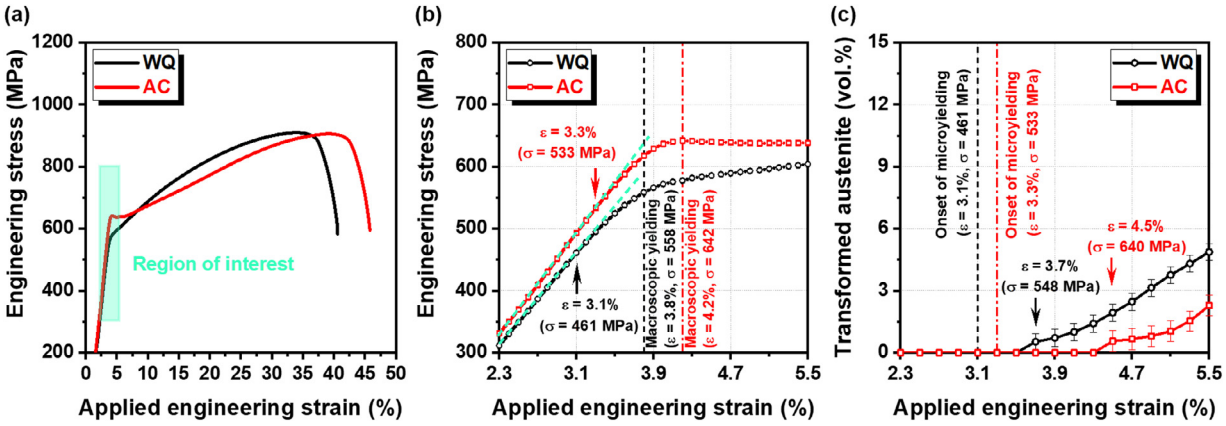

Fig. 7. (a) Engineering stress-strain curves of the water-quenched (WQ) and air-cooled (AC) specimens (acquired from the stress rig used in the *in situ* synchrotron high-energy X-ray diffraction experiments, note that no extensometer was used here and the strain was determined from the crosshead displacement); (b) Magnified region from the region of interest in (a), showing the change in the slope of the engineering stress-strain curves (the arrows indicate the start of the curves' deviation from linearity); (c) The amount of transformed austenite as a function of applied engineering strain (the arrows indicate the onset of the austenite to α'-martensite phase transformation).

Table 4
Summary of characteristic mechanical strength indicators for the water-quenched (WQ) and air-cooled (AC) samples obtained from standard specimens (gauge length 20 mm and width 6 mm) and sub-sized specimens used in the synchrotron high-energy X-ray diffraction (HEXRD) experiments (gauge length 12 mm and width 2 mm). ($R_{p0.2}$ is the 0.2% offset yield strength; R_{eH} is the upper yield strength; R_m is the ultimate tensile strength, R_e^{Bulk} is the microyielding stress of the bulk material determined by the start of the tensile curve's deviation from elastic linearity; R_{crit}^{γ} and R_{crit}^{α} are the critical stress for the onset of plastic deformation in austenite and ferrite, respectively, determined by the deformation-driven change in the weighted average lattice strain.)

Strength (MPa)	Standard specimen			Sub-sized specimen (in HEXRD experiments)				
	$R_{p0.2}$	R_{eH}	R_m	$R_{p0.2}$	R_{eH}	R_e^{Bulk}	R_{crit}^{γ}	R_{crit}^{α}
WQ	556±14	n.a.	858±5	558	n.a.	461	461	525
AC	n.a.	656±17	851±22	n.a.	642	533	533	604

The tensile curves of the two samples acquired from the stress rig during HEXRD experiments are shown in Fig. 7(a). It is worth noting that no extensometer was used here thus the strain value was determined by the crosshead displacement. In addition, a sub-sized tensile specimen (gauge length 12 mm and width 2 mm) was used in the HEXRD experiments. These two factors led to some differences between the tensile curves in Figs. 7(a) and 6(a), with respect to the elongation value and the slope in the elastic deformation stage. Nevertheless, the difference in yield strength between the two samples and their different yielding phenomena were not affected by the specimen size or the instrumental conditions. The major focus here was to investigate the initiation of plastic deformation, hence the analysis of the HEXRD data was confined to the applied engineering strain below 5.5%. This part of the tensile curves is magnified and shown in Fig. 7(b). Both curves showed a deviation from linearity at certain stress values before the macroscopic yield points (the upper yield point for the AC sample and the 0.2% offset yield point for the WQ sample). This deviation marked the occurrence of microyielding, i.e. some grains with favorable conditions started to be plastically deformed while others were still in the elastic deformation regime. The critical stress values for the occurrence of microyielding was determined to be 461 MPa (3.1% applied strain) for the WQ specimen and 533 MPa (3.3% applied strain) for the AC specimen, as summarized in Table 4. At these critical values, deformation-induced austenite to α'-martensite transformation had not yet occurred in either specimen, as shown in Fig. 7(c). In fact, α'-martensite formation only occurred near or beyond the macroscopic yield point at much higher stress values (Fig. 7(c)), i.e. 548 MPa (3.7% applied strain) for the WQ specimen and 640 MPa (4.5% applied strain) for the AC specimen. Therefore, the onset of plastic deformation (microyielding) in both samples should not be affected by austenite-to-martensite phase transformation, but rather resulting from the nucleation and gliding of dislocations. Within the analyzed deformation regimes (below 5.5% strain), no evident asymmetry of the BCC diffraction peaks was observed due to peak overlapping between ferrite and α'-martensite. This was due to the small amount of α'-martensite formation at this deformation stage (below 4.9 vol.% and 2.5 vol.% for the WQ and AC specimens, respectively) and its low carbon concentration. The latter was essentially the same as the carbon content in the parent austenite (~0.44 at.%), which could only result in a small tetragonality of the martensite crystal lattice (c/a = ~1.005) [47].

The change in lattice strain for each crystallographic reflection in the two specimens as a function of applied engineering strain is shown in Fig. 8(a) and (c). The values of four reflections for austenite (γ_{111}, γ_{200}, γ_{220}, and γ_{331}) and three reflections for ferrite (α_{110}, α_{200}, and α_{211}) are presented. The lattice strain evolution of individual crystallographic planes differed from each other in the elastic regime, as suggested by their different slopes shown in Fig. 8(a) and (c). These differences could be explained by the elastic anisotropy of the cubic crystallographic structure [38]. Nevertheless, both specimens showed a common feature, namely, the lattice strain of all crystallographic planes in austenite showed an earlier change in slope (deviating from linearity) than the lattice strain in ferrite (Fig. 8(a) and (c)). This observation suggested that in both samples, austenite was plastically softer than ferrite, thus the onset of plastic deformation occurred first in the austenite grains. The results concur well with the findings reported for other medium-Mn steels with a similar microstructure [16,48].

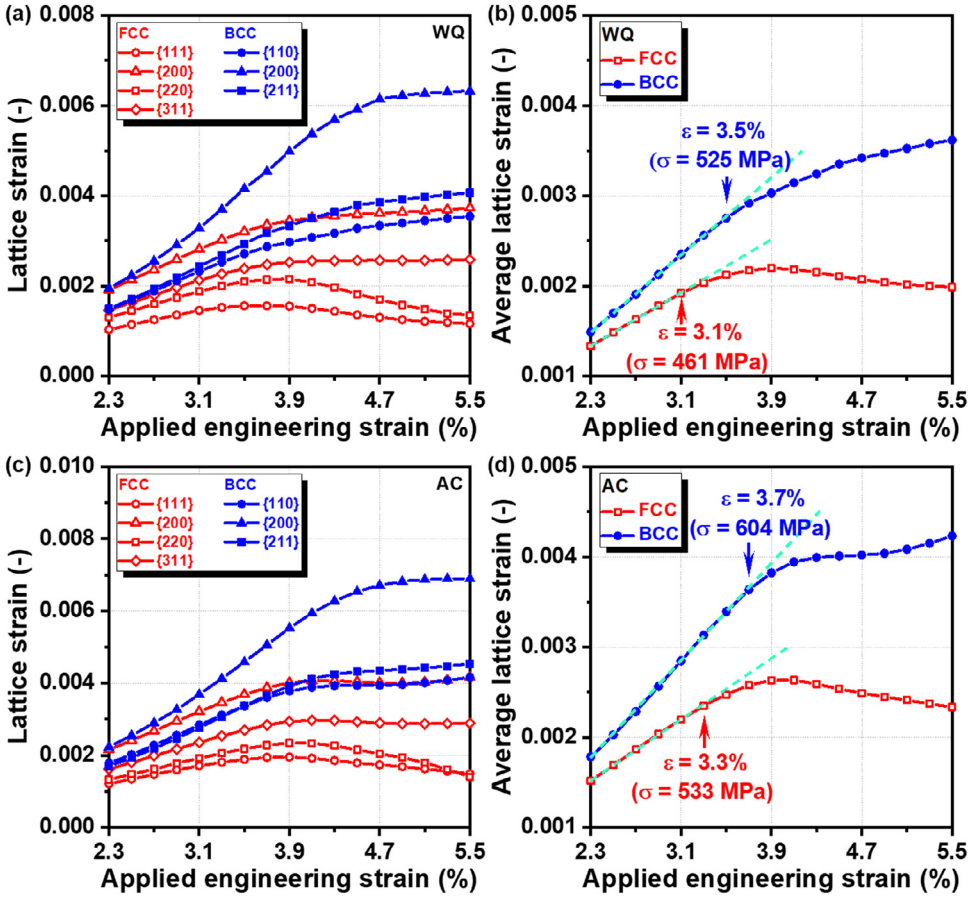

Fig. 8. Lattice strain of individual crystallographic reflection planes as a function of applied engineering strain for (a) the water-quenched (WQ) specimen and (c) the air-cooled (AC) specimen; (b) and (d) Weighted average lattice strain of individual phases in the WQ and AC specimens, respectively (the arrows indicate the start of the curves' deviation from linearity).

The weighted average lattice strain for each phase was calculated based on Eq. 2. The results for the WQ and AC specimens are shown in Fig. 8(b) and (d), respectively. The point of the onset of plastic deformation (microyielding), suggested by the start of the curve's deviation from linearity, was determined for each phase in the two specimens and the corresponding critical stresses are also summarized in Table 4. For both specimens, the microyielding of austenite occurred at the same stress level as the bulk microyielding point, suggesting that the microyielding of the two samples was mainly controlled by the plastic deformation of austenite. Nevertheless, the macroscopic strength should be influenced by both phases, as both phases showed evidence of plastic deformation below the macroscopic yield point. Compared with the WQ specimen, it was observed that both austenite and ferrite in the AC specimen yielded at a higher stress level, i.e. 461 MPa for γ and 525 MPa for α in the WQ specimen vs. 533 MPa for γ (an increase by ~72 MPa) and 604 MPa for α (an increase by ~79 MPa) in the AC specimen. This observation revealed that both phases in the AC sample were less prone to plastically deform, in agreement with the material's higher macroscopic yield resistance. A slight decrease in the lattice strain of austenite was observed after macroscopic yielding in both samples ($>$ 4.1% applied strain and $>$ 4.3% applied strain for the WQ and AC specimens, respectively, Fig. 8). This result indicated a stress relaxation in austenite, which could be due to the load partitioning (redistribution) between ferrite and austenite [49,50] and/or the formation of deformation-induced martensite [16,51]. The latter introduces an internal compressive stress on austenite, counteracting the tensile stress.

3.5. Deformation micromechanisms of the individual phases

To further study the deformation micromechanisms of each phase in the yielding stage, *ex situ* correlative EBSD and ECCI experiments were performed. The two samples were gradually stressed into the microplastic regime, i.e. up to 550 MPa for the WQ specimen (macroscopic yield strength 556 MPa) and 650 MPa for the AC specimen (macroscopic yield strength 656 MPa). Their microstructural evolution upon different tensile stress levels is demonstrated in Figs. 9 and 10. For each specimen, two typical probing areas are presented, one focusing on austenite and the other on ferrite.

In the WQ specimen, prior to deformation, there were a few grown-in stacking faults in austenite and dislocations in ferrite, as shown in Fig. 9(a) and (d). When the sample was stressed to 550 MPa, both phases were found to be plastically deformed, as evidenced by the appearance of new stacking faults in austenite and new dislocations in ferrite (Fig. 9(b) and (e)). The fraction of plastically deformed grains was estimated to be 72% for austenite and 23% for ferrite, based on ECCI observations where in total 82 austenite grains and 52 ferrite grains were analyzed. In many cases, the plastic deformation of austenite and ferrite was driven by dislocation nucleation at the α-γ phase boundaries and their further gliding into the grain interiors. Such preferable dislocation nucleation behavior at the phase boundaries was directly observed by ECCI (Fig. 9(c) and (f)) and also reflected by an increase in local misorientation at the phase boundaries areas (see the kernel average misorientation (KAM) maps in Fig. 9(b) and (e)). Inside the austenite grain, a perfect dislocation readily dissociated

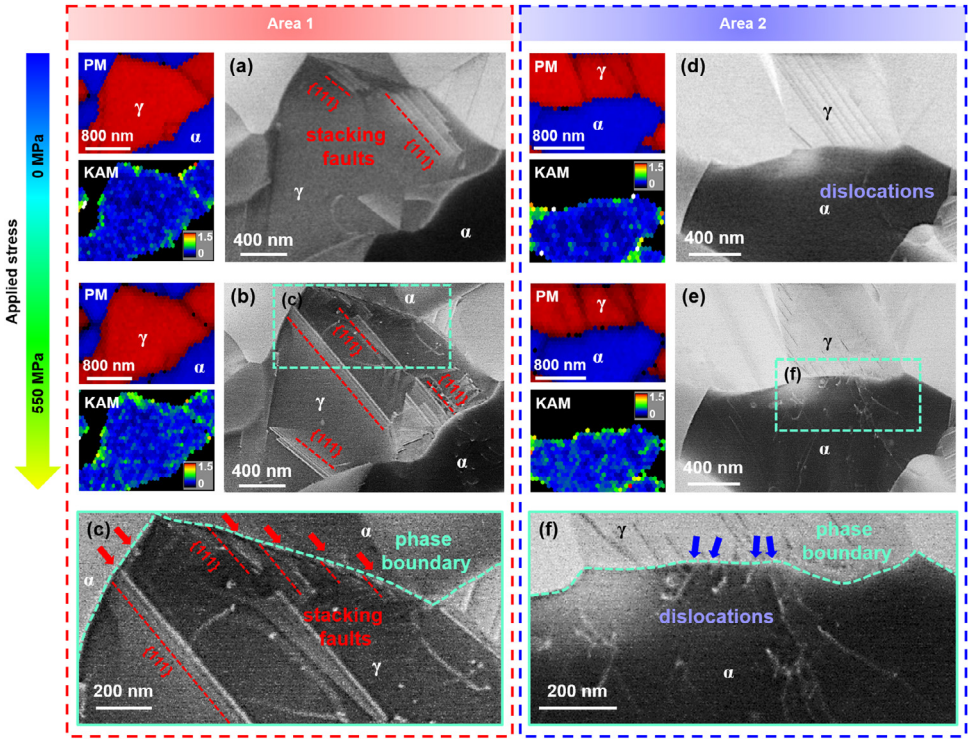

Fig. 9. Microstructure evolution of the water-quenched (WQ) specimen upon tensile loading investigated by correlative electron backscattered diffraction and electron channeling contrast imaging: (a) and (d) microstructure prior to the deformation; (b) and (e) microstructure at the tensile stress of 550 MPa; (c) and (f) the corresponding magnified regions in (b) and (e). (PM stands for phase map and KAM for kernel average misorientation; the arrows in (c) and (f) indicate several dislocation nucleation sites at the ferrite-austenite phase boundaries.)

into two partial dislocations due to the low stacking fault energy (~11 mJ/m^2 [31]) and their gliding resulted in the extension of stacking faults. EBSD plane trace analysis showed that the gliding of these partial dislocations proceeded along the {111} planes.

In comparison to the WQ specimen, a similar deformation feature was observed in the AC specimen, namely, preferable dislocation nucleation at the α-γ phase boundaries for both austenite and ferrite (Fig. 10(e) and (j)), when exposing the sample to a stress of 650 MPa, i.e. slightly below the macroscopic yield point (656 MPa). However, at 550 MPa, where most austenite grains yielded in the WQ specimen, only a small portion of austenite grains (22% out of in total 85 probed grains) was plastically deformed in the AC specimen (Fig. 10(c)) and no plastic deformation inside ferrite was observed (in total 47 probed grains, Fig. 10(h) as one example). These observations matched well with the microyielding stress of the two phases in the AC specimen, i.e. 533 MPa for austenite and 604 MPa for ferrite determined by *in situ* HEXRD.

The above results showed that the initiation of plastic deformation in both samples was driven by dislocation nucleation at the α-γ phase boundaries. Different cooling procedures employed here did not alter such yielding mechanism, but rather affected the critical stress for phase boundary dislocation nucleation. This dislocation nucleation process is obviously more difficult for the AC specimen.

4. Discussion

The results presented in Section 3 showed that most microstructural features (phase constituents, fractions, grain sizes, and grain morphologies) of the investigated medium-Mn steel remained unchanged upon the different cooling procedures (water quenching vs. air cooling) after intercritical annealing. This means that the major microstructural difference between the WQ and AC samples was the carbon segregation at the ferrite-austenite phase boundaries. In this section, we first discuss the origin of this strong segregation. Then we correlate the phase boundary segregation with the observed microscopic and macroscopic strengthening effect in the AC specimen. This correlation provides novel insights into the strategy for future microstructure design, which is discussed in the last part of this section.

4.1. Influence of the cooling rate on carbon segregation at the phase boundary

The absence of carbon segregation at the α-γ phase boundaries in the WQ sample in the investigated material agreed well with previous reports on other medium-Mn steels subjected to intercritical annealing (above 750 °C) and rapid cooling [52,53]. This result suggested that the isothermal holding at the intercritical temperature (here 700 °C) did not result in obvious equilibrium segregation of carbon at phase boundaries. It also indicated that the cooling rate of water quenching (~205 °C/s) was high enough to preserve the carbon concentration profile formed during intercritical annealing at 700 °C. Non-equilibrium segregation, which depends on the formation of vacancy-solute complexes and their diffusion towards interfaces during cooling [54], is not supposed to play a vital role in the current case. At the relatively modest annealing temperature applied here (700 °C), the formation of a sufficiently large concentration of vacancies is not likely [54]. Thus, the observed pronounced carbon segregation at the phase boundaries in the AC sample is attributed to its lower cooling rate (Fig. 1), which provided a wide time window for carbon diffusion towards interfaces during cooling.

More specifically, there are two possible thermodynamic driving forces for such carbon segregation. One is similar to the driving force for equilibrium segregation at grain boundaries [55,56], which is due to the requirement for the reduction of the interfacial energy as formalized in terms of the classical Gibbs adsorption

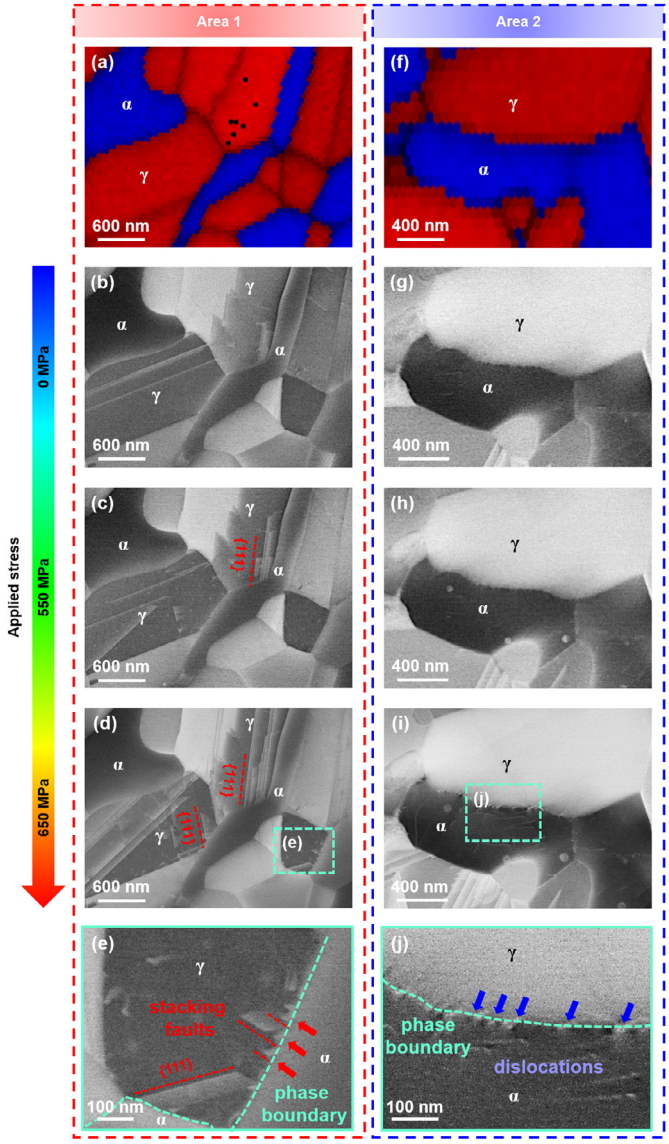

Fig. 10. Microstructure evolution of the air-cooled (AC) specimen upon tensile loading: (a) and (f) phase maps of the selected areas; (b) and (g) microstructure prior to the deformation; (c) and (h) microstructure at the tensile stress of 550 MPa; (d) and (i) microstructure at the tensile stress of 650 MPa; (e) and (j) the corresponding magnified regions in (d) and (i). (The arrows in (e) and (j) indicate several dislocation nucleation sites at the ferrite-austenite phase boundaries.)

isotherm [55,56]. In this case, a difference in the chemical potential of carbon between the phase boundaries and the crystal lattices results in the segregation of carbon atoms towards the phase boundaries. Carbon segregation to grain boundaries has been observed in both ferritic and austenitic steels [28,57–60]. The carbon concentration at α-α grain boundaries can be much higher than the carbon solubility inside of the ferrite grains, namely by a factor of ~10^4 [59,60]. However, the segregation amount depends on the chemical potential of a solute element in the bulk and in the interface, which can be greatly different for individual systems. Also, the carbon segregation coefficient at γ-γ grain boundaries is usually relatively low, of the order of ~10^1 [57]. The accurate interfacial energy for the α-γ phase boundaries is not well known, and depends on the chemical composition and details of the distortion of the crystal structures of the adjacent phases, as well as their orientation relationship, etc. [61]. Even though the segregation amount in the current case is not that high, the equilibrium segregation could occur at such phase boundaries, i.e. we do not rule out that a certain thermodynamic equilibrium segregation trend may apply in the current case. To further justify such a possibility, the investigated steel was intercritically annealed at a lower temperature (550 °C) for 10 hours, followed by rapid cooling (cooling rate > 200 °C/s), as a decrease in the annealing temperature could result in a higher degree of equilibrium interfacial segregation [62]. The carbon profile across the α-γ phase boundary is shown in Fig. S1 (supplementary material). A clear carbon spike was observed at the phase boundary. This result denoted that the equilibrium segregation of carbon, driven by the reduction of the interfacial energy, does occur in the case of the phase boundaries.

The other driving force lies in the trend for carbon partitioning across the α-γ phase boundaries to maintain local equilibrium during air cooling [44,63]. Such a driving force can be rationalized based on the temperature dependence of elemental partitioning between the two phases. We performed the thermodynamic calculation to predict the equilibrium elemental partitioning (including both interstitial and substitutional elements) between austenite and ferrite. The calculation was implemented using the Thermo-Calc software in conjunction with the TCFE9 database. The nominal composition Fe-11.7Mn-2.9Al-0.064C (in wt.%) was employed, and carbides were not included as they were not observed experimentally. It should be noted that for solute partitioning, especially for substitutional elements (here Mn and Al), it is difficult to achieve equilibrium during the air-cooling process. Therefore, the calculation here only provides a thermodynamic background and serves as a qualitative assessment to rationalize the possible driving force of the observed carbon segregation at the phase boundaries.

The equilibrium carbon content in austenite and ferrite as a function of temperature is shown in Fig. 11. It shows that the carbon partitioned into austenite at equilibrium increases at lower temperatures (Fig. 11 (a)). When considering kinetics, due to the high mobility of carbon in ferrite, carbon atoms can diffuse quickly to the interface, and a local equilibrium of carbon could be approached at the α-γ phase boundaries. However, the much lower diffusivity of carbon inside austenite (more than five orders of magnitude lower than carbon diffusivity in ferrite [64]) limited its diffusion out of the interface regions. In some extreme cases, e.g. when the diffusion occurs at modest temperatures (i.e. during air cooling), this confined region could become very narrow and appear as a spike with the width of only a few nanometers. Such partitioning-driven enrichment of solute atoms at interphase boundaries was also referred to as segregation by Bruggeman and Kula [46].

It is worth pointing out that studies of phase boundary segregation are scarce in the literature [61,65], and the application of segregation theories (i.e. equilibrium and non-equilibrium segregation) in phase boundary segregation requires further systematic investigations. The treatment for such types of hetero-interfaces differs from that for grain boundaries, due to their very different structures, chemistry, and interfacial energy. Therefore, fundamental research needs to be conducted in this field to further elucidate the mechanisms of phase boundary segregation.

4.2. Phase boundary segregation-induced strengthening and discontinuous yielding

Next, we discuss the influence of phase boundary segregation of carbon on the yielding behavior in the investigated steel. Before addressing this point, it is worthwhile to mention that the increase in yield strength and the occurrence of discontinuous yielding have not only been observed in the current duplex medium-Mn steel subjected to slow cooling. These phenomena are also often observed in some low-carbon steels with a single-phase ferritic microstructure after static strain aging [66,67], typically ex-

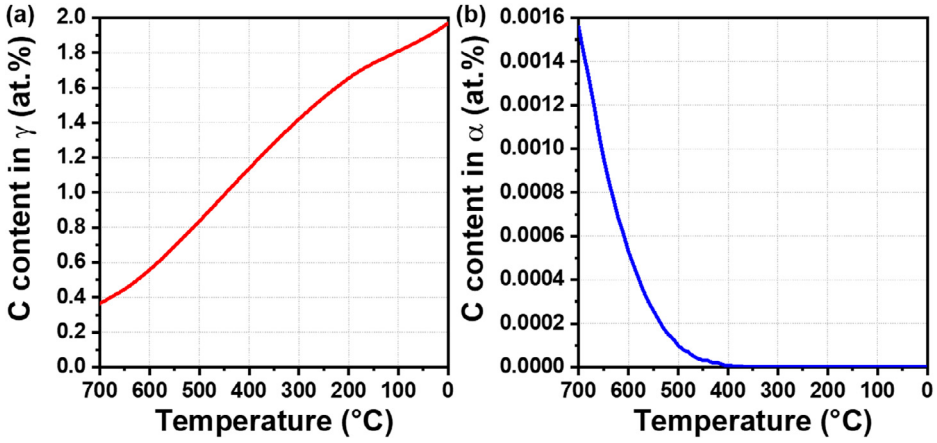

Fig. 11. Equilibrium concentration of carbon in (a) γ-austenite and (b) α-ferrite in the steel Fe-11.7Mn-2.9Al-0.064C (in wt.%) as a function of temperature from 700 °C down to 0 °C, calculated by the Thermo-Calc software using the TCFE9 database.

plained by the Cottrell-Bilby theory [68], that is, the interaction between dislocations and interstitial carbon atoms. During aging, interstitial atoms tend to diffuse into the distorted dislocation cores and lock the grown-in dislocations in position. A higher stress is thus required to unlock these anchored dislocations and initiate the plastic flow. Indeed, these possible carbon-dislocation interactions could not be fully eliminated in the current AC sample, even though no evident carbon segregation at dislocations was observed in the probed APT tips. However, when applying the Cottrell-Bilby theory to explain the observed increase in yield strength in the AC sample, we encountered several difficulties, which are listed as follows.

i The Cottrell mechanism increases the yield strength in the circumstances when the materials' plastic deformation is initiated by the gliding of grown-in dislocations. However, this situation is different from our observation in the investigated medium-Mn steel, where the plastic deformation of many austenite and ferrite grains was driven by dislocation nucleation at the α-γ phase boundaries and their further gliding into the grain interiors (Section 3.5). Such preferable dislocation nucleation at phase boundaries in the investigated steel is most likely due to the ultrafine grain size [69,70], which can suppress dislocation generation from Frank-Read sources due to the reduced dislocation segment length and the strong influence of dislocation back stresses [71]. This ultrafine grain-induced interfacial dislocation emission has also been documented and discussed in other alloys (e.g. pure Al [69], interstitial-free steels [72], and high-Mn austenitic steels [70]), where interstitial elements are either absent or interacting only weakly with dislocations.

ii The results in Sections 3.4 and 3.5 showed that the observed enhancement of the macroscopic yield strength in the AC sample was due to the more reluctant plastic deformation in both ferrite and austenite. HEXRD results revealed that the air cooling increased the critical stress for the plastic deformation in austenite by a similar level (~72 MPa) compared with that of ferrite (~79 MPa). Such a high level of strength increase for austenite could not be explained by solute-dislocation interactions. It was reported that the interaction between carbon and dislocations in austenite is very weak, i.e. with a binding energy of only ~0.015 eV much lower than that in ferrite (~0.8 eV) [73,74]. Other possible solute-defect interactions inside austenite, such as the Suzuki effect which describes substitutional element (e.g. Mn) segregation to stacking faults, are also unlikely to markedly influence the strength level. This point is supported by some investigations on high-Mn austenitic steels [30,75]. Kang et al. [30] compared the tensile properties of a Fe-28Mn-0.3C steel (grain size ~16 μm) subjected to either water quenching or air cooling and observed only a small increase in yield strength by ~15 MPa in the air-cooled sample. Wesselmecking et al. [75] performed a bake-hardening treatment (at 170 °C for up to 30 min) on a Fe-19Mn-2Cr-1Al-0.4C steel (grain size ~3 μm) and found that the resulting strength increase was almost negligible for a small pre-strain level (e.g. 2%).

These aspects suggest that the Cottrell mechanism, which is generally used to explain the yield strength increase in coarse-grained ferritic steels after slow cooling or bake-hardening treatment, could not be adopted as a cause in the current ultrafine-grained duplex medium-Mn steel. We thus believe that the primary reason for the higher yield strength in the AC sample lies in the carbon segregation at the ferrite-austenite phase boundaries, which increases the critical stress for dislocation nucleation at these interface regions. In this context, the yielding of austenite and ferrite can be influenced by a similar degree (Table 4), as the initiation of plastic deformation in both phases relies on such a dislocation nucleation event (Section 3.5).

It has been proposed for single-phase materials that the dislocation sources at grain boundaries could be grain boundary dislocations [76,77] or grain boundary ledges [77,78]. The accumulation of solute atoms at theses source regions might stabilize them, making dislocation nucleation at grain boundaries more difficult [27-29]. This point has been used by some researchers to correlate solute element segregation at random high-angle grain boundaries in single-phase steels with the observed increase in the Hall-Petch coefficient K_y [27–30]. The latter has been proposed to be associated with the energy (or critical stress) required to emit dislocations from grain boundaries [79]. As dislocations and ledges also exist inside phase boundaries [80], the above explanation can also be extended to the situation of phase boundary segregation. From an atomistic point of view, molecular dynamics simulations suggest that dislocation emission from interfaces is associated with a local reshuffling of the atoms inside the interfaces [81]. This rearrangement can be hindered by a strong interaction between the solvent and the segregating atoms, suggesting that a higher energy barrier for dislocation nucleation has to be overcome [81,82]. The strong interaction between carbon and iron atoms was rationalized by *ab initio* calculations [83], which revealed that carbon enhanced the localization of electrons at the iron atoms and assisted the covalent character of interatomic bonds between iron and carbon. Another explanation for the suppressed interface dislocation

emission due to carbon segregation comes from the work of Kang et al. [84] and Wesselmecking et al. [75]. They proposed that Mn-C short-range ordering (SRO) can form in high-Mn steels and serve as obstacles against dislocation glide upon yielding. In this context, the accumulation of carbon atoms at or near phase boundaries might promote the formation of Mn-C SRO at these regions, thus a higher stress would be required for the interface dislocation nucleation process.

The above-proposed strengthening mechanism, i.e. carbon segregation at the phase boundaries and its effect on the increase in the critical stress for dislocation nucleation at these interface regions, can also be used to explain the observed discontinuous yielding phenomenon in the AC sample. In single-phase materials with ultrafine grain size (e.g. pure Al [69], interstitial-free steels [72], and high-Mn austenitic steels [70]), discontinuous yielding is normally attributed to the high area fraction of interfaces which can act as both sinks and sources for dislocations [85]. Dislocation nucleation from interface sources (e.g. ledges) requires to overcome an energy barrier [78], which means that the stress for nucleating dislocations is higher than that for further dislocation gliding. Such stress difference constitutes an important contribution to the abrupt and rapid plastic flow avalanches, promoting the occurrence of discontinuous yielding [16,27]. The current investigated steel contained a relatively low carbon content (0.064 wt.%), which also ensured a low carbon concentration at the phase boundaries if no segregation occurred (i.e. the WQ sample). In this case, the energy barrier for phase boundary dislocation emission might not be high enough to result in significant plastic flow avalanches. Thus, a continuous yielding behavior was prevalent in the WQ sample. In contrast, air cooling promoted carbon segregation at the phase boundaries. This could effectively enhance the energy barrier of dislocation emission and thus the stress difference between dislocation nucleation and gliding, which transformed the yielding behavior of the AC sample to a discontinuous manner even though the bulk composition was not changed.

The above discussion complements our current understanding of discontinuous yielding in ultrafine-grained duplex medium-Mn steels [16], by adding the point that besides dislocation nucleation at phase boundaries and its further multiplication, the chemistry of the phase boundary itself also plays a vital role in the occurrence of discontinuous yielding. In the literature, discontinuous plastic yielding has been frequently reported in medium-Mn steels with elevated carbon content (above ~0.10 wt.% [86]) even in the water-quenched state (i.e. where carbon segregation at the phase boundaries is not expected). In these medium-Mn steels, the carbon concentration at the phase boundaries is supposed to be intrinsically high enough to trigger discontinuous yielding even without pronounced interfacial carbon segregation. Nevertheless, the degree of discontinuous yielding in these steels can further be amplified by additional phase boundary segregation. To give an example, we show the tensile curves of another medium-Mn steel (Fe-10.4Mn-2.9Al-0.185C, in wt.% [87]) subjected to intercritical annealing (750 °C for 5 min) followed by either water quenching or air cooling (Fig. 12). Similarly, this 0.185C medium-Mn steel also possessed an ultrafine-grained ferrite-austenite duplex microstructure (austenite fraction ~47 vol.%, average grain size 0.34 μm for γ and 0.39 μm for α in the water-quenched sample) [87]. It was expected that the air cooling applied for this material also resulted in carbon segregation at the ferrite-austenite phase boundaries. This steel showed a discontinuous yielding regardless of the cooling procedures. However, the value of the yield drop (the difference between upper and lower yield strength) was much higher for the air-cooled sample (~96 MPa) compared with its water-quenched counterpart (~38 MPa, Fig. 12). In addition, this steel also showed an increased yield strength by ~120 MPa after air cooling. This result thus provided an additional case, supporting the influence of phase boundary segregation on enhancing yield strength and promoting discontinuous yielding in medium-Mn steels.

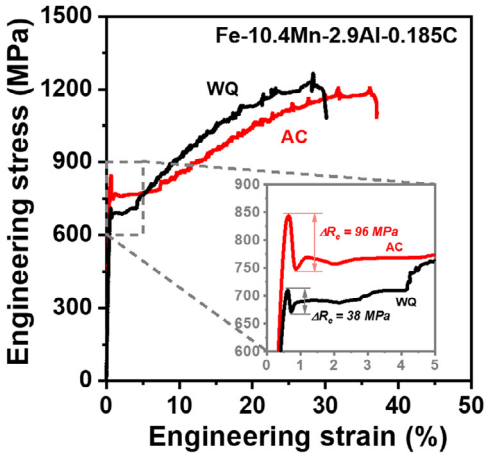

Fig. 12. Quasi-static tensile property of a high carbon-containing medium-Mn steel (Fe-10.4Mn-2.9Al-0.185C, in wt.%) subjected to cold rolling and intercritical annealing at 750 °C for 5 min, followed by either water quenching (WQ) or air cooling (AC).

4.3. Implications on future microstructural design of multiphase materials

Solute element decoration at interfaces can sometimes significantly influence the macroscopic mechanical properties of metallic materials. Some types of impurity segregation weakens the interface and can even cause intergranular fracture in steels, for instance, the temper embrittlement phenomenon caused by phosphorous segregation at grain boundaries [55]. In contrast, boron segregation at ferrite or prior-austenite grain boundaries can replace the phosphorous segregation and effectively enhance interface cohesive strength, resulting in better toughness [88]. Manipulating such solute decoration to improve materials' mechanical performance has been considered as a successful microstructural engineering approach and is referred to as segregation engineering [56]. However, the previous application and discussion of this approach has been limited to grain boundaries [56] or twin boundaries [89]. Here we show, for the first time, that carbon segregation at hetero-interfaces (i.e. the ferrite-austenite phase boundaries) can also result in the enhancement of the yield strength of steels, demonstrated here exemplarily through an increase by ~100 MPa for a Fe-11.7Mn-2.9Al-0.064C steel and by ~120 MPa for a Fe-10.4Mn-2.9Al-0.185C steel. Such a phase boundary segregation-induced strengthening effect augments the arsenal of interfacial segregation engineering mechanisms. In this respect, the engineering of phase boundary segregation might be even more readily feasible and more flexible than conventional grain boundary segregation (which usually follows the Gibbs adsorption isotherm, i.e. it is an equilibrium segregation by nature), as it can be facilitated and accelerated by solute element partitioning between adjacent phases. This aspect means that such a type of kinetically governed interface segregation can be adjusted over a wide range, depending on heat treatment and cooling protocols, unbound by the Gibbs adsorption isotherm. The present study thus generally highlights the importance of phase boundaries and their intrinsic characteristics, particularly their chemistry, revealing a novel and very efficient tool for microstructure manipulation.

5. Conclusions

In the present work, the influence of carbon segregation at the ferrite-austenite phase boundaries on the yielding behavior in

ultrafine-grained duplex medium-Mn steels was systematically investigated. The main conclusions are summarized as follows:

- We found that different cooling conditions (i.e. water quenching and air cooling) after intercritical annealing strongly affected the behavior of carbon segregation at the ferrite-austenite phase boundaries. The water-quenched sample did not show evidence of carbon segregation, while air cooling resulted in a pronounced carbon spike at the phase boundaries, with the value (~1.48 at.%) about five times higher than the nominal carbon content (0.29 at.%) of the material. Other microstructural features including phase constituents, fractions, grain sizes, and morphologies remained unchanged upon the different cooling procedures.
- The sharp carbon enrichment at phase boundaries in the air-cooled sample was attributed to the slow cooling rate, especially at low temperatures (below 400 °C). This provided sufficient time for carbon diffusion to the interfaces, which could be driven by the requirement for the reduction of the interfacial energy and particularly the carbon partitioning across the ferrite-austenite phase boundaries to maintain local equilibrium. For the latter case, the limited carbon diffusivity in austenite inhibited carbon diffusion out of the interface regions, thus confining its enrichment to the nearest trap, viz., the phase boundaries.
- The phase boundary segregation of carbon resulted in a substantial increase in the yield strength by 100–120 MPa and simultaneously promoted discontinuous yielding. In particular, the segregation in the low-carbon medium-Mn steel (Fe-11.7Mn-2.9Al-0.064C, in wt.%) transformed its yielding from a continuous behavior to a discontinuous pattern.
- A combination of *in situ* synchrotron high-energy X-ray diffraction and *ex situ* electron channeling contrast imaging experiments revealed that carbon segregation at the ferrite-austenite phase boundaries impeded dislocation emission at these interfaces, causing a higher stress level for activating dislocation nucleation and initiating the plastic flow in both phases. The more difficult plastic deformation of both phases thus led to the observed higher yield strength in the air-cooled sample. The observation also suggests that the presence of carbon at phase boundaries enhances the energy barrier for dislocation nucleation. This can provide a more favorable condition for plastic flow avalanches, thus promoting discontinuous yielding.
- This study complements the current understanding of discontinuous yielding behavior in medium-Mn steels, by adding the point that besides dislocation nucleation at phase boundaries and its further multiplication, the chemistry of the phase boundary itself also plays a vital role in the occurrence of discontinuous yielding. The findings also shed light on future microstructural design strategies in multiphase metallic materials, by showing how to utilize and manipulate phase boundary segregation to improve mechanical performance. A special feature of the chemical manipulation of hetero-interfaces through such partitioning effects is, that it is not bound by the Gibbs adsorption limit (such as for the case of classical grain boundary segregation) but can be adjusted over a wide range of decoration states, depending on the diffusion coefficients of the adjacent phases, the thermal treatment and the cooling conditions.

6. Funding

This work was supported by the Deutsche Forschungsgemeinschaft (DFG) within the Collaborative Research Centre (SFB) 761 “Steel - *ab initio*”.

Declaration of Competing Interest

The authors declare that they have no known competing financial interests or personal relationships that could have appeared to influence the work reported in this paper.

Acknowledgment

Binhan Sun gratefully acknowledges the research fellowship provided by the Alexander von Humboldt Foundation. The synchrotron high-energy X-ray diffraction measurements were carried out at the Powder Diffraction and Total Scattering Beamline P02.1 of PETRA III at DESY (Proposal No.: I-20191072), a member of the Helmholtz Association (HGF), which is gratefully acknowledged. Mr. Simon Evertz and Dr. Martin Etter are gratefully acknowledged for their support of acquiring HEXRD data. Dr. Baptiste Gault is sincerely acknowledged for fruitful discussions on the APT results.

Supplementary materials

Supplementary material associated with this article can be found, in the online version, at doi:10.1016/j.actamat.2020.09.007.

References

[1] N. Fonstein, Advanced High Strength Sheet Steels - Physical Metallurgy, Design, Processing, and Properties, Springer International Publishing, AG, Basel, 2015.
[2] D.K. Matlock, J.G. Speer, E. De Moor, P.J. Gibbs, Recent developments in advanced high strength sheet steels for automotive applications: An overview, JESTECH 15 (2012) 1–12.
[3] O. Bouaziz, H. Zurob, M. Huang, Driving force and logic of development of advanced high strength steels for automotive applications, Steel Res. Int 84 (2013) 937–947.
[4] D. Raabe, C.C. Tasan, E.A. Olivetti, Strategies for improving the sustainability of structural metals, Nature 575 (2019) 64–74.
[5] J.-H. Schmitt, T. Iung, New developments of advanced high-strength steels for automotive applications, C. R. Physique 19 (2018) 641–656.
[6] W. Bleck, S. Papaefthymiou, A. Frehn, Microstructure and tensile properties in dual phase and TRIP steels, Steel Res. Int 75 (2004) 704–710.
[7] P. Jacques, F. Delannay, X. Cornet, P. Harlet, J. Ladriere, Enhancement of the mechanical properties of a low-carbon, low-silicon steel by formation of a multiphased microstructure containing retained Austenite, Metall. Mater. Trans. A 29 (1998) 2383–2393.
[8] R. Rana, P.J. Gibbs, E. De Moor, J.G. Speer, D.K. Matlock, A composite modeling analysis of the deformation behavior of medium manganese steels, Steel Res. Int 86 (2015) 1139–1150.
[9] B.C. De Cooman, Structure–properties relationship in TRIP steels containing carbide-free bainite, Curr. Opin. Solid State Mater. Sci 8 (2004) 285–303.
[10] W. Bleck, F. Brühl, Y. Ma, C. Sasse, Materials and processes for the third-generation advanced high-strength steels, BHM 164 (2019) 466–474.
[11] Y. Toji, H. Matsuda, M. Herbig, P.-P. Choi, D. Raabe, Atomic-scale analysis of carbon partitioning between martensite and austenite by atom probe tomography and correlative transmission electron microscopy, Acta Mater. 65 (2014) 215–228.
[12] X. Zhang, T. Hickel, J. Rogal, S. Fähler, R. Drautz, J. Neugebauer, Structural transformations among austenite, ferrite and cementite in Fe–C alloys: A unified theory based on ab initio simulations, Acta Mater. 99 (2015) 281–289.
[13] N. Ishikawa, K. Yasuda, H. Sueyoshi, S. Endo, H. Ikeda, T. Morikawa, K. Higashida, Microscopic deformation and strain hardening analysis of ferrite–bainite dual-phase steels using micro-grid method, Acta Mater. 97 (2015) 257–268.
[14] Z.H. Cong, N. Jia, X. Sun, Y. Ren, J. Almer, Y.D. Wang, Stress and strain partitioning of ferrite and martensite during deformation, Metall. Mater. Trans. A 40 (2009) 1383–1387.
[15] C.C. Tasan, M. Diehl, D. Yan, C. Zambaldi, P. Shanthraj, F. Roters, D. Raabe, Integrated experimental–simulation analysis of stress and strain partitioning in multiphase alloys, Acta Mater. 81 (2014) 386–400.
[16] B. Sun, Y. Ma, N. Vanderesse, R.S. Varanasi, W. Song, P. Bocher, D. Ponge, D. Raabe, Macroscopic to nanoscopic in situ investigation on yielding mechanisms in ultrafine grained medium Mn steels: Role of the austenite-ferrite interface, Acta Mater. 178 (2019) 10–25.
[17] C.C. Tasan, M. Diehl, D. Yan, M. Bechtold, F. Roters, L. Schemmann, C. Zheng, N. Peranio, D. Ponge, M. Koyama, K. Tsuzaki, D. Raabe, An overview of dual-phase steels: Advances in microstructure-oriented processing and micromechanically guided design, Annu. Rev. Mater. Res 45 (2015) 391–431.
[18] Q. Lai, O. Bouaziz, M. Gouné, L. Brassart, M. Verdier, G. Parry, A. Perlade, Y. Bréchet, T. Pardoen, Damage and fracture of dual-phase steels: Influence of martensite volume fraction, Mater. Sci. Eng. A 646 (2015) 322–331.

[19] B. Sun, D. Palanisamy, D. Ponge, B. Gault, F. Fazeli, C. Scott, S. Yue, D. Raabe, Revealing fracture mechanisms of medium manganese steels with and without delta-ferrite, Acta Mater. 164 (2019) 683–696.
[20] H.K.D.H. Bhadeshia, Prevention of hydrogen embrittlement in steels, ISIJ Int. 56 (2016) 24–36.
[21] B. Sun, W. Krieger, M. Rohwerder, D. Ponge, D. Raabe, Dependence of hydrogen embrittlement mechanisms on microstructure-driven hydrogen distribution in medium Mn steels, Acta Mater. 183 (2020) 313–328.
[22] D.-W. Suh, S.-J. Kim, Medium Mn transformation-induced plasticity steels: Recent progress and challenges, Scripta Mater. 126 (2017) 63–67.
[23] Y.K. Lee, J. Han, Current opinion in medium manganese steel, Mater. Sci. Technol 31 (2015) 843–856.
[24] Y. Ma, Medium-manganese steels processed by austenite-reverted-transformation annealing for automotive applications, Mater. Sci. Technol 33 (2017) 1713–1727.
[25] R.L. Miller, Ultrafine-grained microstructures and mechanical properties of alloy-steels, Metall. Trans 3 (1972) 905–912.
[26] J. Shi, J. Hu, C. Wang, C.Y. Wang, H. Dong, W.Q. Cao, Ultrafine grained duplex structure developed by ART-annealing in cold rolled medium-Mn steels, J. Iron Steel Res. Int. 21 (2014) 208–214.
[27] S. Takaki, D. Akama, N. Nakada, T. Tsuchiyama, Effect of grain boundary segregation of interstitial elements on Hall-Petch coefficient in steels, Mater. Trans 55 (2014) 28–34.
[28] B. Mintz, H. Ke, G.D.W. Smith, Grain size strengthening in steel and its relationship to grain boundary segregation of carbon, Mater. Sci. Technol 8 (1992) 537–540.
[29] D. Akama, N. Nakada, T. Tsuchiyama, S. Takaki, A. Hironaka, Discontinuous yielding induced by the addition of nickel to interstitial-free steel, Scripta Mater. 82 (2014) 13–16.
[30] J.-H. Kang, S. Duan, S.-J. Kim, W. Bleck, Grain boundary strengthening in high Mn austenitic steels, Metall. Mater. Trans. A 47 (2016) 1918–1921.
[31] Y. Ma, W. Song, S. Zhou, A. Schwedt, W. Bleck, Influence of intercritical annealing temperature on microstructure and mechanical properties of a cold-rolled medium-Mn steel, Metals 8 (2018) 357.
[32] Y. Ma, Processes, microstructure, and mechanical properties of cold-rolled medium-Mn steel, Verlagshaus Mainz GmbH Aachen, Aachen, 2020.
[33] I. Gutierrez-Urrutia, S. Zaefferer, D. Raabe, Coupling of electron channeling with EBSD: Toward the quantitative characterization of deformation structures in the SEM, JOM 65 (2013) 1229–1236.
[34] A.C. Dippel, H.P. Liermann, J.T. Delitz, P. Walter, H. Schulte-Schrepping, O.H. Seeck, H. Franz, Beamline P02.1 at PETRA III for high-resolution and high-energy powder diffraction, J. Synchrotron Radiat 22 (2015) 675–687.
[35] A. Hammersley, FIT2D: a multi-purpose data reduction, analysis and visualization program, J. Appl. Crystallogr. 49 (2016) 646–652.
[36] L. Lutterotti, Total pattern fitting for the combined size–strain–stress–texture determination in thin film diffraction, Nucl. Instrum. Meth. B 268 (2010) 334–340.
[37] Y. Ma, W. Song, W. Bleck, Investigation of the microstructure evolution in a Fe-17Mn-1.5Al-0.3C steel via in situ synchrotron X-ray diffraction during a tensile test, Materials 10 (2017) 1129.
[38] K. Yan, K.-D. Liss, I.B. Timokhina, E.V. Pereloma, In situ synchrotron X-ray diffraction studies of the effect of microstructure on tensile behavior and retained austenite stability of thermo-mechanically processed transformation induced plasticity steel, Mater. Sci. Eng. A 662 (2016) 185–197.
[39] T. Furukawa, H. Huang, O. Matsumura, Effects of carbon content on mechanical properties of 5%Mn steels exhibiting transformation induced plasticity, Mater. Sci. Technol. 10 (1994) 964–970.
[40] E.V. Pereloma, I.B. Timokhina, M.K. Miller, P.D. Hodgson, Three-dimensional atom probe analysis of solute distribution in thermomechanically processed TRIP steels, Acta Mater. 55 (2007) 2587–2598.
[41] H.-W. Yen, S.W. Ooi, M. Eizadjou, A. Breen, C.-Y. Huang, H.K.D.H. Bhadeshia, S.P. Ringer, Role of stress-assisted martensite in the design of strong ultrafine–grained duplex steels, Acta Mater. 82 (2015) 100–114.
[42] N. Vandijk, A. Butt, L. Zhao, J. Sietsma, S. Offerman, J. Wright, S. van der Zwaag, Thermal stability of retained austenite in TRIP steels studied by synchrotron X-ray diffraction during cooling, Acta Mater. 53 (2005) 5439–5447.
[43] E. De Moor, D.K. Matlock, J.G. Speer, M.J. Merwin, Austenite stabilization through manganese enrichment, Scripta Mater 64 (2011) 185–188.
[44] O. Dmitrieva, D. Ponge, G. Inden, J. Millán, P. Choi, J. Sietsma, D. Raabe, Chemical gradients across phase boundaries between martensite and austenite in steel studied by atom probe tomography and simulation, Acta Mater. 59 (2011) 364–374.
[45] O.C. Hellman, J.A. Vandenbroucke, J. Rüsing, D. Isheim, D.N. Seidman, Analysis of Three-dimensional Atom-probe Data by the Proximity Histogram, Microsc. Microanal. 6 (2000) 437–444.
[46] G. Bruggeman, E.B. Kula, Segregation at interphase boundaries, in: J.J. Burke, N.L. Reed, V. Weiss (Eds.), Surfaces and Interfaces II, Springer, Boston, MA, 1968, pp. 455–480.
[47] V.A. Lobodyuk, Y.Y. Meshkov, E.V. Pereloma, On tetragonality of the martensite crystal lattice in steels, Metall. Mater. Trans. A 50 (2018) 97–103.
[48] S. Lee, S. Shin, M. Kwon, K. Lee, B.C. De Cooman, Tensile properties of medium Mn steel with a bimodal UFG $\alpha + \gamma$ and coarse δ-ferrite microstructure, Metall. Mater. Trans. A 48 (2017) 1678–1700.
[49] M. Zhang, L. Li, J. Ding, Q. Wu, Y.-D. Wang, J. Almer, F. Guo, Y. Ren, Temperature-dependent micromechanical behavior of medium-Mn transformation-induced-plasticity steel studied by in situ synchrotron X-ray diffraction, Acta Mater. 141 (2017) 294–303.
[50] R. Shi, Z. Nie, Q. Fan, G. Li, Elastic plastic deformation of TC6 titanium alloy analyzed by in-situ synchrotron based X-ray diffraction and microstructure based finite element modeling, J. Alloys Compd. 688 (2016) 787–795.
[51] P.J. Gibbs, B.C. De Cooman, D.W. Brown, B. Clausen, J.G. Schroth, M.J. Merwin, D.K. Matlock, Strain partitioning in ultra-fine grained medium-manganese transformation induced plasticity steel, Mater. Sci. Eng. A 609 (2014) 323–333.
[52] S. Lee, K. Lee, B.C. De Cooman, Observation of the TWIP + TRIP plasticity-enhancement mechanism in Al-added 6 wt pct medium Mn steel, Metall. Mater. Trans. A 46 (2015) 2356–2363.
[53] S. Lee, B.C. De Cooman, Tensile behavior of intercritically annealed ultra-fine grained 8% Mn multi-phase steel, Steel Res. Int. 86 (2015) 1170–1178.
[54] R.G. Faulkner, Non-equilibrium grain-boundary segregation in austenitic alloys, J. Mater. Sci. 16 (1981) 373–383.
[55] H.J. Grabke, Surface and grain-boundary segregation on and in iron, Steel Res. 57 (1986) 178–185.
[56] D. Raabe, M. Herbig, S. Sandlöbes, Y. Li, D. Tytko, M. Kuzmina, D. Ponge, P.-P. Choi, Grain boundary segregation engineering in metallic alloys: A pathway to the design of interfaces, Current Opin. Solid State Mater. Sci. 18 (2014) 253–261.
[57] M. Tomozawa, Y. Miyahara, K. Kako, Solute segregation on $\Sigma 3$ and random grain boundaries in type 316L stainless steel, Mater. Sci. Eng. A 578 (2013) 167–173.
[58] M. Herbig, M. Kuzmina, C. Haase, R.K.W. Marceau, I. Gutierrez-Urrutia, D. Haley, D.A. Molodov, P. Choi, D. Raabe, Grain boundary segregation in Fe–Mn–C twinning-induced plasticity steels studied by correlative electron backscatter diffraction and atom probe tomography, Acta Mater. 83 (2015) 37–47.
[59] P. Lejček, Grain Boundary Segregation In Meta, Springer, Berlin, Heidelberg, 2010.
[60] D. Raabe, S. Sandlöbes, J. Millán, D. Ponge, H. Assadi, M. Herbig, P.-P. Choi, Segregation engineering enables nanoscale martensite to austenite phase transformation at grain boundaries: A pathway to ductile martensite, Acta Mater. 61 (2013) 6132–6152.
[61] P. Lejček, S. Hofmann, Thermodynamics and structural aspects of grain boundary segregation, Critical Rev. Solid State Mater. Sci. 20 (1995) 1–85.
[62] J.M. Papazian, D.N. Besherb, Grain boundary segregation of carbon in iron, Metall. Trans 2 (1971) 497–503.
[63] H. Kamoutsi, E. Gioti, G.N. Haidemenopoulos, Z. Cai, H. Ding, Kinetics of solute partitioning during intercritical annealing of a medium-Mn steel, Metall. Mater. Trans. A 46 (2015) 4841–4846.
[64] L. Yuan, D. Ponge, J. Wittig, P. Choi, J.A. Jiménez, D. Raabe, Nanoscale austenite reversion through partitioning, segregation and kinetic freezing: Example of a ductile 2GPa Fe–Cr–C steel, Acta Mater. 60 (2012) 2790–2804.
[65] M. Enomoto, 5 - Structure, energy and migration of phase boundaries in steels, in: E. Pereloma, D.V. Edmonds (Eds.), Phase Transformations in Steels, Woodhead Publishing, Cambridge, UK, 2012, pp. 157–183.
[66] D.V. Wilson, B. Russell, The contribution of atmosphere locking to the strain-ageing of low carbon steels, Acta Metall. 8 (1960) 36–45.
[67] L.J. Baker, S.R. Daniel, J.D. Parker, Metallurgy and processing of ultralow carbon bake hardening steels, Mater. Sci. Technol. 18 (2013) 355–368.
[68] A.H. Cottrell, B.A. Bilby, Dislocation theory of yielding and strain ageing of iron, Proc. Phys. Soc. A 62 (1949) 49–62.
[69] C.Y. Yu, P.W. Kao, C.P. Chang, Transition of tensile deformation behaviors in ultrafine-grained aluminum, Acta Mater. 53 (2005) 4019–4028.
[70] S. Kang, J.-G. Jung, M. Kang, W. Woo, Y.-K. Lee, The effects of grain size on yielding, strain hardening, and mechanical twinning in Fe–18Mn–0.6C–1.5Al twinning-induced plasticity steel, Mater. Sci. Eng. A 652 (2016) 212–220.
[71] G. Gottstein, Physical Foundations of Materials Science, Springer, Heidelberg, 2004.
[72] S.S. Hazra, E.V. Pereloma, A.A. Gazder, Microstructure and mechanical properties after annealing of equal-channel angular pressed interstitial-free steel, Acta Mater. 59 (2011) 4015–4029.
[73] M.S. Blanter, I.S. Golovin, R. De Batist, S.A. Golovin, Effect of plastic deformation on the carbon internal friction peak in austenitic steels, Phys. Status Solidi A 178 (2000) 621–632.
[74] Y.Z. Li, Z.C. Luo, Z.Y. Liang, M.X. Huang, Effect of carbon on strain-rate and temperature sensitivity of twinning-induced plasticity steels: Modeling and experiments, Acta Mater. 165 (2019) 278–293.
[75] S. Wesselmecking, W. Song, Y. Ma, T. Roesler, H. Hofmann, W. Bleck, Strain aging behavior of an austenitic high-Mn steel, Steel Res. Int 89 (2018) 1700515.
[76] M.A. Tschopp, D.L. McDowell, Grain boundary dislocation sources in nanocrystalline copper, Scripta Mater. 58 (2008) 299–302.
[77] J.P. Hirth, R.W. Balluffi, On grain boundary dislocations and ledges, Acta Metall. 21 (1973) 929–942.
[78] L.E. Murr, Dislocation ledge sources: dispelling the myth of Frank–Read source importance, Metall. Mater. Trans. A 47 (2016) 5811–5826.
[79] V. Bata, E.V. Pereloma, An alternative physical explanation of the Hall–Petch relation, Acta Mater. 52 (2004) 657–665.
[80] J.H. van der Merwe, G.J. Shiflet, The role of structural ledges at phase boundaries—I. Interfaces with rectangular atomic nets, Acta Metall. Mater. 42 (1994) 1173–1187.
[81] V. Borovikov, M.I. Mendelev, A.H. King, Effects of solutes on dislocation nucleation from grain boundaries, Int. J. Plast 90 (2017) 146–155.

[82] V. Borovikov, M.I. Mendelev, A.H. King, Solute effects on interfacial dislocation emission in nanomaterials: Nucleation site competition and neutralization, Scripta Mater. 154 (2018) 12–15.
[83] V.G. Gavriljuk, V.N. Shivanyuk, B.D. Shanina, Change in the electron structure caused by C, N and H atoms in iron and its effect on their interaction with dislocations, Acta Mater. 53 (2005) 5017–5024.
[84] J.-H. Kang, T. Ingendahl, J. von Appen, R. Dronskowski, W. Bleck, Impact of short-range ordering on yield strength of high manganese austenitic steels, Mater. Sci. Eng. A 614 (2014) 122–128.
[85] D.V. Wilson, Role of grain boundaries in the discontinuous yielding of low-carbon steels, Met. Sci. J 1 (1967) 40–47.
[86] B.C. De Cooman, P. Gibbs, S. Lee, D.K. Matlock, Transmission electron microscopy analysis of yielding in ultrafine-grained medium Mn transformation-induced plasticity steel, Metall. Mater. Trans. A 44 (2013) 2563–2572.
[87] B. Sun, F. Fazeli, C. Scott, N. Brodusch, R. Gauvin, S. Yue, The influence of silicon additions on the deformation behavior of austenite-ferrite duplex medium manganese steels, Acta Mater. 148 (2018) 249–262.
[88] M. Sharma, I. Ortlepp, W. Bleck, Boron in heat-treatable steels: A review, Steel Res. Int. 90 (2019) 1900133.
[89] J.F. Nie, Y.M. Zhu, J.Z. Liu, X.Y. Fang, Periodic segregation of solute atoms in fully coherent twin boundaries, Science 340 (2013) 957–960.